NEW MEASUREMENTS OF THE RADIO PHOTOSPHERE OF MIRA BASED ON DATA FROM THE JVLA AND ALMA

The Astrophysical Journal, 808:36 (10pp), 2015 July 20 doi:10.1088/0004-637X/808/1/36

NEW MEASUREMENTS OF THE RADIO PHOTOSPHERE OF MIRA BASED ON DATA FROM THE JVLA AND ALMA

L. D. Matthews[1], M. J. Reid[2], and K. M. Menten[3]
[1] MIT Haystack Observatory, Off Route 40, Westford, MA 01886, USA; lmatthew@haystack.mit.edu
[2] Harvard-Smithsonian Center for Astrophysics, 60 Garden Street, MS-42, Cambridge, MA 02138, USA
[3] Max-Planck-Institut für Radioastronomie, Auf dem Hügel 69, D-53121 Bonn, Germany
Received 2015 March 16; accepted 2015 June 9; published 2015 July 16

ABSTRACT

We present new measurements of the millimeter wavelength continuum emission from the long period variable Mira (*o* Ceti) at frequencies of 46, 96, and 229 GHz ($\lambda \approx 7$, 3, and 1 mm) based on observations obtained with the Jansky Very Large Array (JVLA) and the Atacama Large Millimeter/submillimeter Array (ALMA). The measured millimeter flux densities are consistent with a radio photosphere model derived from previous observations, where flux density $S_\nu \propto \nu^{1.86}$. The stellar disk is resolved, and the measurements indicate a decrease in the size of the radio photosphere at higher frequencies, as expected if the opacity decreases at shorter wavelengths. The shape of the radio photosphere is found to be slightly elongated, with a flattening of ∼10%–20%. The data also reveal evidence for brightness non-uniformities on the surface of Mira at radio wavelengths. Mira's hot companion, Mira B was detected at all three observed wavelengths, and we measure a radius for its radio-emitting surface of $\approx 2.0 \times 10^{13}$ cm. The data presented here highlight the power of the JVLA and ALMA for the study of the atmospheres of evolved stars.

Key words: stars: AGB and post-AGB – stars: atmospheres – stars: fundamental parameters – stars: imaging

1. INTRODUCTION

Mira (*o* Ceti) is the archetype of its class of long-period variable stars and is one of the most extensively studied stars in the Galaxy. Mira has an oxygen-rich chemistry and is undergoing mass loss at a rate of $\sim 2 \times 10^{-7}\, M_\odot$ yr^{-1} (Ryde & Schöier 2001).[4] The pulsation period of Mira is 332 days, during which the visible light of the star varies by up to ∼8 mag. Mira is also a member of the nearest symbiotic binary system, Mira AB. The companion, Mira B, has a projected separation of ∼0.″5 (55 AU; Karovska et al. 1997; Ramstedt et al. 2014) and is likely to be a white dwarf (Sokoloski & Bildsten 2010).

Both components of the Mira AB binary are detectable at radio wavelengths (Matthews & Karovska 2006). Matthews & Karovska showed that the radio emission from Mira B is consistent with free–free emission originating from an ionized circumstellar region $\sim 10^{13}-10^{14}$ cm in radius. Based on measurements of the flux density $S_{B,\nu}$ between 8.5 and 43.3 GHz, they derived a fit to the radio spectrum of the form $S_{B,\nu} = (0.010 \pm 0.008)\nu_{\rm GHz}^{1.18\pm0.28}$ mJy.

The radio emission from Mira A has an origin quite different from its companion. Reid & Menten (1997; hereafter RM97) showed that the centimeter wavelength emission detected from Mira A and other nearby, long-period variables can be explained by the existence of a "radio photosphere" with a radius approximately twice that of the classical photospheric radius $R_\star$ (defined by the line-free regions of the optical-infrared spectrum). For Mira-type variables, $R_\star$ is typically ∼1–2 AU, while between ∼1–2$R_\star$ is a molecular layer (Perrin et al. 2004) that may be nearly opaque in the visible and infrared. The radio photosphere thus lies adjacent to this molecular layer.

The emission arising from the radio photosphere has a spectral index $\alpha \approx 2$ (consistent with optically thick blackbody emission) all the way from centimeter to submillimeter wavelengths. However, the flux densities over this spectral range are roughly a factor of two higher than expected from an extrapolation of the optical photospheric emission. Based on the model developed by RM97, the dominant source of opacity in the radio photosphere is the interaction between free electrons (mostly from ionization of K and Na) and neutral H and H_2. At millimeter and centimeter wavelengths, unity optical depth is achieved at a radius of ∼3–4 AU, where the density and temperature are $\sim 10^{12}$ cm^{-3} and ≈1600 K, respectively.

The detection and characterization of radio photospheres in asymptotic giant branch (AGB) stars provide a new tool for the investigation of the critical region between the classic photosphere and the dust formation zone where the stellar wind is launched. In oxygen-rich AGB stars, the radio photosphere also lies just interior to the atmospheric region where SiO masers arise, and contemporaneous observations of these maser lines provide additional diagnostics of the density, temperature, dynamics, and shock propagation within this complex and important atmospheric region (RM97; Gray et al. 2009). As noted by RM97, red giants with well-characterized radio photospheres may also be useful as calibration sources in the millimeter and submillimeter regimes.

The characteristic sizes and temperatures of radio photospheres imply that resolved imaging observations are within the reach of current radio interferometers for nearby stars. Using the Very Large Array (VLA) of the National Radio Astronomy Observatory[5] in its highest resolution configuration, Reid & Menten (2007) obtained resolved images of three oxygen-rich long-period variables (including Mira) at a wavelength of

[4] Throughout the paper we adopt a distance of 110 ± 9 pc (Haniff et al. 1995), based on the period-luminosity relation of Feast et al. (1989).

[5] The National Radio Astronomy Observatory (NRAO) is a facility of the National Science Foundation operated by Associated Universities, Inc. under cooperative agreement with the National Science Foundation.

7 mm, while Menten et al. (2012) resolved the carbon star IRC+10216. One intriguing finding from these studies is evidence that the radio photospheres in some cases appear distinctly non-circular. However, since observations were available at only a single epoch and at a single point during the stellar pulsation cycle, it was difficult to distinguish between possible origins for these observed shapes, and it is unknown whether the shapes are static or time-variable.

The exquisite continuum sensitivity of the recently upgraded Jansky VLA (JVLA; Perley et al. 2011) and the Atacama Large Millimeter/submillimeter Array (ALMA; Wootten & Thompson 2009) now provide a tremendous leap in our ability to obtain high-quality images of radio photospheres over a broad range of wavelengths. At 7 mm, the continuum sensitivity of the JVLA exceeds that of the pre-upgrade VLA by an order of magnitude. At the same time ALMA supplies sub-mJy sensitivity with only modest integration times, and its longest baselines are capable of providing angular resolution comparable to, or higher than the JVLA, depending on observing frequency. Here we present an analysis of new observations of Mira obtained with the JVLA and ALMA at wavelengths of 7 mm (46 GHz) 3 mm (96 GHz), and 1 mm (229 GHz). The quality of the data underscore the potential of these two instruments for the study of stellar atmospheres. All of the data were obtained during the course of a nine-month period (i.e., during a timescale less than a single stellar pulsation cycle) in 2014.

2. OBSERVATIONS

2.1. JVLA Data

Observations of Mira at 46 GHz (7 mm) were carried out with the JVLA in its most extended (A) configuration (0.68–36.4 km baselines) on 2014 February 23 during a 3 hr observing session. Data were recorded with 2 s integration times. Offset corrections as refinements to the reference antenna pointing model were evaluated hourly using observations of a strong point source at 8 GHz. 3C48 was observed as an absolute flux calibrator, and the bright continuum source J0359+5057 (NRAO150) was observed as a bandpass calibrator.

To obtain maximum continuum sensitivity, a 3 bit observing mode was employed, and the WIDAR correlator was configured with four baseband pairs tuned to contiguously cover the frequency range from 41.8–49.4 GHz with dual circular polarizations. Each baseband pair contained 16 subbands, each with a bandwidth of 128 MHz and 128 spectral channels. This frequency range included the SiO $v = 1$ and $v = 2$, $J = 1$–0 maser transitions (see below). The total on-source integration time for Mira was approximately 1 hr 51 minutes, split into two observing blocks that were bracketed by observations of the gain (amplitude and phase) calibrator J0215–0222.

2.2. ALMA Data

ALMA observations of Mira were performed in Band 3 (94 GHz) on 2014 October 17 and 25 and in Band 6 (229 GHz) on 2014 October 29 and November 1, respectively, using an array configuration with baselines up to 15.2 km. The data were obtained by ALMA staff for science verification purposes (ALMA Partnership 2015) and were released to the public in 2015 February. A total of 38 (39) antennas were present in the array for the Band 3 (6) observations. The total on-source integration times for Mira were approximately 1.6 hr in Band 3 and 1.1 hr in Band 6. Data from the different observing dates were combined for each band for the present analysis.

3. DATA PROCESSING

3.1. JVLA Data

Data processing for the JVLA data was performed using the Astronomical Image Processing System (AIPS; Greisen 2003), taking into account special considerations necessary for handling JVLA data as outlined in Appendix E of the AIPS Cookbook.[6]

The data were loaded into AIPS directly from archival science data model format (ASDM) files using the Obit software package (Cotton 2008). The default calibration ("CL") table was then recreated to update the single-dish antenna gain curve and atmospheric opacity corrections.

After updating the antenna positions and flagging obviously corrupted data, a requantizer gain correction was applied, as required for three bit data. Next, a fringe fit was performed using one minute of data from the observation of J0359+5057 to correct the instrumental delay settings. Separate delay solutions were determined for each of the four independent basebands. Bandpass calibration was performed using NRAO150, assuming a spectral index of $\alpha = 0.4$ (Trippe et al. 2010). The absolute flux density scale was calculated using the latest time-dependent flux density values for 3C48 from Perley & Butler (2013). The resulting flux density S_ν as a function of frequency for 3C48 is therefore given by $\log(S_\nu) = 1.3324 - 0.7690(\log(\nu)) - 0.1950(\log(\nu))^2 + 0.059(\log(\nu))^3$, where ν is the frequency expressed in GHz. The frequency-independent portion of the complex gains (amplitude and phase) was calibrated using J0215–0222 to remove possible slow (hour timescale) instrumental gain drifts. Additionally, a correction of $-3''.324$ in DEC was applied to the observed (J2000.0) position of Mira to account for the large proper motion of the star. This was required after the discovery that corrections for parallax and proper motion were inadvertently excluded from the source position entered in the observation scheduling file.

Mira is a well-known source of SiO maser emission (e.g., Cotton et al. 2006; McIntosh & Bonde 2010). We therefore employed the method developed by Reid & Menten (1990) to improve the phase calibration using the stellar maser signal. After completion of the initial calibration steps described above, the spectral channel containing the brightest SiO $v = 1$, $J = 1$–0 maser emission was split from the main data set, and several iterations of phase-only self-calibration were performed on the maser data until convergence was reached. From these solutions, phase corrections appropriate for each of the 64 subbands comprising the full 8 GHz bandwidth of the continuum measurements were derived using the AIPS task SNP2D. (Effectively, the phase correction $\phi_{\nu'}$ for a given subband with central frequency ν' then becomes $\phi_{\nu'} = (\nu'/\nu_0)\phi_0$, where ν_0 is the frequency of the reference channel and ϕ_0 is the computed phase correction in that channel.) If the maser emission is sufficiently strong, in principle this approach allows achievement of nearly perfect "seeing" in the resulting continuum measurements (Reid &

[6] http://www.aips.nrao.edu/cook.html

Menten 1990; RM97). However, at the phase Mira was observed, the SiO masers were in a relatively low state (integrated flux density ~2.7 Jy), and the modest signal-to-noise ratio (S/N) on some of the longest baselines was a limiting factor in the calibration solutions (see appendix).

After applying the derived phase corrections, a second round of self-calibration was performed on the reference channel, this time solving for both the amplitudes and the phases. To mitigate possible drift in the amplitudes, the gains were normalized during this step, and the resulting change in the amplitude scale was measured to be less than 0.5%. Once these gain corrections had been applied to the full data set, spectral channels 1–3 and 125–128 of each subband (where noise is significantly higher) were flagged, along with spectral channels containing line emission. Next, the data were averaged to a time resolution of 10 s to reduce the data volume and Hanning smoothed to reduce ringing caused by the narrow maser lines. At this stage, optimized weights for the visibility data were computed using the AIPS task REWAY, and finally, the data were further averaged in frequency, resulting in 8 spectral channels in each of the 64 subbands.

3.2. ALMA Data

We retrieved the pipeline calibrated *u*–*v* data in the form of CASA measurement sets for each of the two ALMA bands from the ALMA Science Verification Data web pages.[7] Details of the processing steps used to produce these data sets are available at that site.

The flux density scale for the Band 3 data taken on October 17 was calibrated using the source J0334–4008, assuming a flux density at 86.2251 GHz of 1.6589 Jy and a spectral index of $\alpha = -0.7146$. For the Band 3 data from October 25, J0238+1636 and J2258–2758 were used as flux density calibrators, assuming, respectively, $S_\nu = 1.8550$ Jy, $\alpha = -0.269071$ and S_ν=1.1315 Jy, $\alpha = -0.7282$. For Band 6, the flux density scale for the October 29 data was set using J0334–4008, assuming $S_\nu = 0.8282$ Jy at 229.5497 GHz and $\alpha = -0.7029$. For the November 01 data, the flux calibrator was J0238+1636, and the adopted values were S_ν =1.3893 Jy and $\alpha = -0.2005$ at 229.5485 GHz.

At this stage, the continuum portion of the Band 3 data included a total of nine spectral windows (three in each of three independent basebands) and dual linear polarizations. Each spectral window contained eight spectral channels (250 MHz each) across a ~1.8 GHz band (i.e., with slight spectral overlap between channels). The frequency ranges sampled were 87.3–89.0, 97.4–99.1, and 99.3–101.0 GHz. The continuum portion of the Band 6 data contained two spectral windows (both within a single baseband), again with dual linear polarizations and eight 250 MHz spectral channels across a ~1.8 GHz total band. The frequency range covered by the Band 6 observations was ~228.7–230.4 GHz.

Using the continuum emission from the Mira AB binary itself, we performed self-calibration on the pipeline data for both ALMA bands. Initially, several iterations of phase-only self-calibration were performed using a solution interval equal to the record length of the data (~6 s in Band 3 and ~3 s in Band 6) until convergence was reached. These solutions were applied, and additional iterations were performed, solving for both amplitude and phase with a solution interval of 60 s. To avoid a possible drift in the amplitudes, the gains were normalized during this latter step, and the resulting change in the amplitude scales of both bands were measured to be <0.7%.

[7] https://almascience.nrao.edu/alma-data/science-verification

Table 1
Deconvolved Image Characteristics

Band	θ_B(maj) (mas)	θ_B(min) (mas)	PA (deg)	θ_R (mas)	rms noise (μJy beam^{-1})
(1)	(2)	(3)	(4)	(5)	(6)
Q (46 GHz)	45	34	–23	39.7	29.0
3 (96 GHz)	79	58	+42	68.7	19.7
6 (229 GHz)	32	23	+19	27.3	34.8

Note. θ_B(maj) and θ_B(min) are the major and minor axis diameters of the synthesized dirty beam measured at FWHM using "robust 0" weighting of the visibilities. The position angle (PA) of the beam is measured east from north. Deconvolved images used for the present analysis used circular restoring beams with FWHM as specified in column 5, and where θ_R is equal to the mean of θ_B(maj) and θ_B(min).

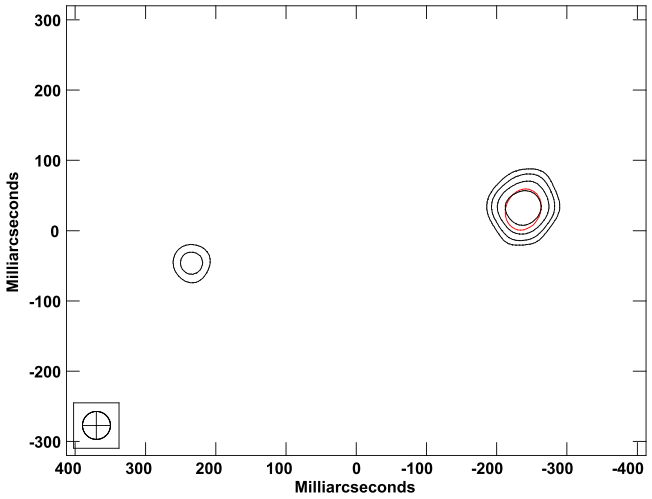

Figure 1. Image of Mira AB obtained with the JVLA at a frequency of 46 GHz on 2014 February 23. Contour levels are (−1 [absent], 1, 2, 4, 8) × 290 μJy beam^{-1}. The lowest contour is 10σ. The restoring beam had a FWHM 39.7 mas. The red ellipse indicates the dimensions of the best uniform elliptical disk fit to the visibility data for Mira A.

3.3. Imaging the Data

Imaging and deconvolution of the JVLA and the ALMA data were performed using IMAGR in AIPS. For the images presented here, we used a Briggs robust value of $\mathcal{R} = 0$, a cell size of 5 mas, and a circular restoring beam with a FWHM equal to the mean of the dimensions of the dirty beam at the appropriate frequency (see Table 1). Corrections were applied during imaging for the frequency dependence of the primary beam and the expected spectral index of Mira A within the JVLA band ($\alpha = 1.86$; RM97). Images of the Mira AB binary at each of the three observed frequencies are presented in Figures 1–3.

4. RESULTS

4.1. The Millimeter Wavelength Flux Densities and Sizes of Mira A and B

4.1.1. Mira A

We have used two approaches to measure the flux density and size of Mira A based on the current data. The first was to fit

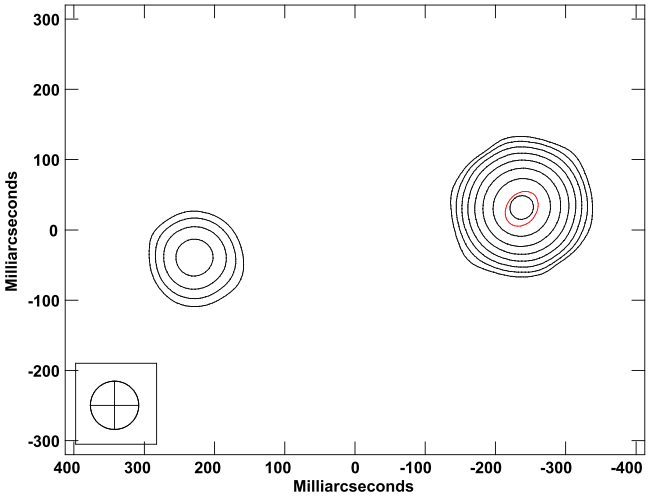

Figure 2. Image of Mira AB obtained from ALMA data at a frequency of 94 GHz. Contour levels are (−1 [absent], 1, 2, 4...128) × 197 μJy beam^{-1}. The lowest contour is 10σ. The restoring beam had a FWHM of 68.7 mas. The red ellipse indicates the dimensions of the best uniform elliptical disk fit to the visibility data for Mira A.

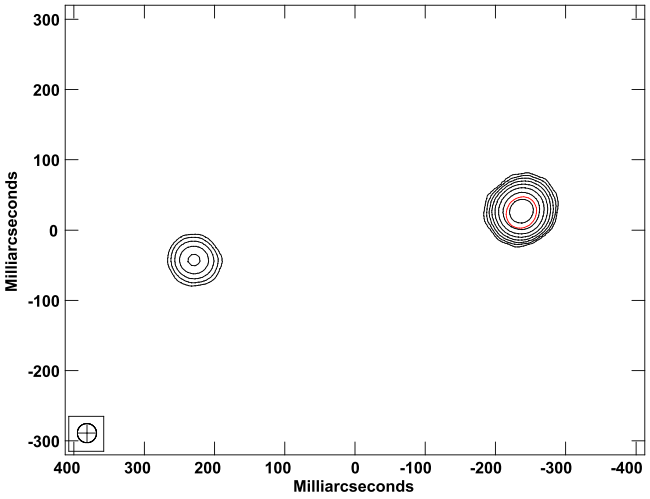

Figure 3. Image of Mira AB obtained from ALMA data at a frequency of 229 GHz. Contour levels are (−1 [absent], 1, 2, 4...128) × 348 μJy beam^{-1}. The lowest contour is 10σ. The restoring beam had a FWHM of 27.3 mas. The red ellipse indicates the dimensions of the best uniform elliptical disk fit to the visibility data for Mira A.

a uniform elliptical disk model to the visibility data at each observed frequency using the AIPS task OMFIT. The results are summarized in the top section of Table 2. The second method was to fit elliptical Gaussians in the image plane using the "robust 0" images summarized in Table 1. General expressions for an elliptical Gaussian and for the visibility amplitude of a uniform disk may be found in Condon (1997) and Pearson (1999), respectively. For a resolved source, the FWHM size measured from an elliptical Gaussian fit (after deconvolution with the size of the dirty beam) is expected to be a factor of 0.625 times the major axis of the elliptical disk fit (Pearson 1999), consistent with our measurements. The derivation of the error bars given in Table 2 is described in the Appendix.

The sizes derived from our uniform elliptical disk fits are overlaid on the contour images presented in Figures 1–3. We have resolved the stellar disk at all three of the observed frequencies. Furthermore, our measurements point to a trend of decreasing size for the radio photosphere with increasing frequency. The arithmetic means of the angular diameters in Table 2 translate to radio photospheric radii of 4.5 × 10^{13} cm (3.0 AU) at 46 GHz, 3.9 × 10^{13} cm (2.6 AU) at 96 GHz, and 3.6 × 10^{13} cm (2.4 AU) at 229 GHz. The radio photosphere model of RM97 predicts that the size of the radio photosphere should decrease at higher frequencies, and this is the first time that this has been confirmed observationally for an AGB star. A similar effect has been previously seen in the red supergiant Betelgeuse (Lim et al. 1998).

The angular sizes that we measure for the radio photosphere are intermediate between values previously measured for the "molecular layer" of Mira in the infrared (Perrin et al. 2004) and the sizes of the SiO $v = 1$ and $v = 2$, $J = 1$–0 maser emitting "rings," whose radii have been found to range between ∼30–40 mas (3.3–4.4 AU) over the course of the stellar pulsation cycle (Cotton et al. 2006). These results suggest that the SiO masers arise just outside the radio photosphere, consistent with previous findings (Reid & Menten 2007; see also Gray et al. 2009). In addition to resolving the photosphere, our new measurements point to a statistically significant elongation in the shape of Mira's radio photosphere at a level of ∼10%–20% (i.e., $\epsilon \approx 0.8-0.9$), with the major axis of the elongation lying along a position angle (PA) between 139° and 156°.

Figure 4 plots the short wavelength radio spectrum of Mira A (and Mira B, discussed below) based on our current measurements. Additional data points at 338 GHz from Ramstedt et al. (2014) are also included. The latter measurements were derived from a combination of ALMA data taken on 2014 February 25 and May 3 with a relatively compact antenna configuration that only marginally resolved the two stars.

The solid line overplotted on Figure 4 is not a fit to the data, but rather represents the flux density as a function of frequency predicted by the radio photosphere model of RM97:

$$S_\nu = 0.50\left(\frac{\nu}{10\ \mathrm{GHz}}\right)^{1.86}\left(\frac{D}{100\ \mathrm{pc}}\right)^{-2}\ \mathrm{mJy}, \qquad (1)$$

where D is the distance to the star in parsecs. We see that this model provides an excellent match to the data for our adopted distance of 110 pc.

Based on the parameters derived from our uniform disk fits, we present in column 8 of Table 2 the brightness temperature, T_b, of Mira computed for each of the three observed frequencies. Although the uncertainties in the derived T_b values are rather large, these values are systematically higher than expected from the radio photosphere model of RM97, which predicts brightness temperatures of ≈1600 K. Our values are also higher than the measurement of $T_b = 1680 \pm 250$ K previously reported for Mira by Reid & Menten (2007). Temperatures higher than those predicted by the RM97 model would imply an increase in opacity owing to more efficient collisional ionization of K, Na, and other low-ionization elements. Consistent with this, the photospheric radii that we measure are systematically smaller than the RM97 model predicts (ignoring uncertainties in the adopted stellar distance).

The brightness temperature measurements in Table 2 represent lower limits to the stellar effective temperature of

Table 2
Measured Photospheric Parameters for Mira A

Band	Stellar Phase	θ_{maj} (mas)	θ_{min} (mas)	PA (degrees)	ϵ	S_ν (mJy)	T_b (K)
(1)	(2)	(3)	(4)	(5)	(6)	(7)	(8)
Values Based on Uniform Elliptical Disk Fits to Visibility Data							
Q (46 GHz)	0.76	60.0 ± 2.0 (0.7)	49.3 ± 1.6 (0.5)	156 ± 4 (1)	0.82 ± 0.04	7.4 ± 1.5 (0.04)	2110 ± 440
3 (96 GHz)	0.47	53.4 ± 11.2 (0.1)	42.3 ± 13.0 (0.1)	142 ± 36 (0.3)	0.79 ± 0.29	34.4 ± 6.9 (0.01)	2900 ± 1200
6 (229 GHz)	0.51	46.2 ± 2.3 (0.03)	41.5 ± 2.3 (0.02)	144 ± 11 (0.1)	0.90 ± 0.07	150 ± 30 (0.04)	2620 ± 560
Values Based on Elliptical Gaussian Fits to Image Data							
Q (46 GHz)	0.76	37.5 ± 2.1 (0.7)	31.7 ± 2.0 (0.7)	147 ± 6 (4)	0.84 ± 0.07	7.6 ± 1.5 (0.07)	...
3 (96 GHz)	0.47	32.8 ± 18.3 (0.2)	26 ± 26(0.2)	139 ± 3 (1)	$0.8^{+0.2}_{-0.8}$	34.4 ± 7.0 (0.04)	...
6 (229 GHz)	0.51	30.4 ± 0.4 (0.03)	27.0 ± 0.4 (0.03)	143.4 ± 0.5 (0.4)	0.89 ± 0.02	153 ± 31 (0.09)	...

Note. Stellar phase was derived using the ephemeris available from the database of the American Association of Variable Star Observers (AAVSO) at http://www.aavso.org. The error bars on the measured quantities include formal, systematic, and calibration uncertainties, as described in the appendix. For measured quantities, the value in parentheses indicates the contribution to the total error budget from the formal fit uncertainties. For a uniform disk, θ_{maj} and θ_{min} are the major and minor axis sizes of the disk, respectively; for a Gaussian fit they represent the the FWHM dimensions of the elliptical Gaussian, after deconvolution with the size of the dirty beam. For a resolved source, θ_{maj} measured from a Gaussian fit is expected to be 0.625 times the value of θ_{maj} measured from a uniform disk fit. The ellipticity, ϵ, is calculated as the ratio of θ_{min} to θ_{maj}. The brightness temperature was computed as $T_b = 2S_\nu c^2/(k\nu^2\pi\theta_{maj}\theta_{min})$, where c is the speed of light and k is the Boltzmann constant.

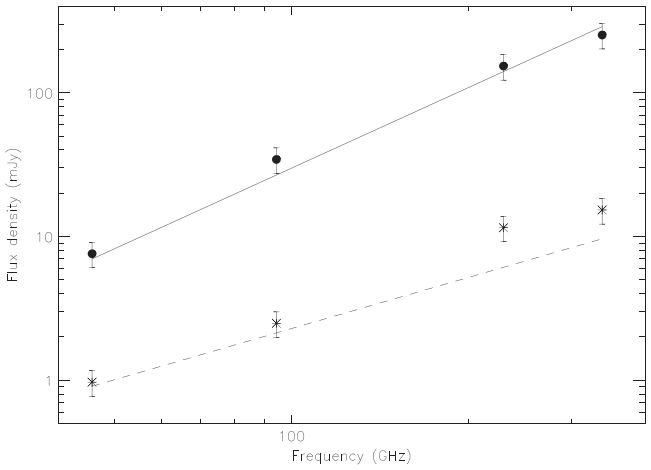

Figure 4. Radio spectra for Mira A (solid points) and Mira B (asterisks). The three lower frequency points are from the present study and the point at 338 GHz is from Ramstedt et al. (2014). Flux densities were derived from fits to image data (Table 2). The solid line is the spectrum predicted for Mira A by the radio photosphere model of RM97 (Equation (2)), and the dashed line is the spectrum derived from earlier measurements of Mira B (between 8 and 43 GHz) from the study of Matthews & Karovska (2006; see Section 1).

Mira, and indeed, we find that they are comparable to, or smaller than most published effective temperature values (e.g., $T_{eff} \sim 2630-2800$ K, Haniff et al. 1995; $T_{eff} \sim 2918-3192$ K, Woodruff et al. 2004). However, the T_b values systematically exceed the temperature of ~2000 K derived for the molecular layer of Mira by Perrin et al. (2004). This is somewhat surprising in light of the expectation that the radio photosphere should lie just exterior to this molecular layer (RM97).

4.1.2. Mira B

Measurements of the millimeter wavelength flux density for Mira B at each of the three observed frequencies are presented in Table 3 and are plotted on the spectrum in Figure 4. We see from Figure 4 that at 46 and 96 GHz, the measured flux densities of Mira B match closely with the relation derived by Matthews & Karovska (2006). However, both of the two higher-frequency measurements lie significant above the relation. The origin of this deviation is unclear. The model developed by Seaquist et al. (1984) and Taylor & Seaquist (1984) for radio emission from symbiotic binaries predicts a flattening or downturn in the flux density at higher frequencies, opposite to the observed trend. Furthermore, the period of the Mira AB binary (~500 years; Prieur et al. 2002) is too long for orbital modulation to have a measurable effect on the spectral index over the course of the one-year period when these data were obtained.

Based on the Gaussian fits presented in Table 3, it is clear that we have resolved the radio surface of Mira B at the highest observed frequency. At 46 GHz, the source also appears to be marginally resolved, although the inferred size is only a fraction of the synthesized beam and the uncertainties are large. At 96 GHz, the inferred size is consistent with being intermediate between the other two bands; however, after consideration of systematic errors, Mira B cannot formally be distinguished from a point source at this frequency.

Based on the ALMA 229 GHz data, we derive a radius for Mira B of $\approx 2.0 \times 10^{13}$ cm. This is many orders of magnitude larger than the expected photospheric radius of a white dwarf. This is therefore consistent with the radio emission arising from thermal bremsstrahlung from an ionization-bounded hyper-compact H II region surrounding Mira B, embedded in Mira A's neutral wind. However, for a canonical electron temperature of 10,000 K, the measured radius is approximately four times larger than the radius that would be required for an optically thick blackbody to yield the measured flux density. This, coupled with the apparent change in spectral index at high frequencies, implies that a more complex model is needed to fully describe the observed short-wavelength radio emission. This is not surprising given the complex environment surrounding the two stars. In particular, Mira A's circumstellar

Table 3
Measured Parameters for Mira B

Band	θ_{maj} (mas)	θ_{min} (mas)	PA (degrees)	S_ν (mJy)
(1)	(2)	(3)	(4)	(5)
Q (46 GHz)	18 ± 5 (4)	11 ± 6 (5)	172 ± 30 (29)	0.97 ± 0.20 (0.05)
3 (96 GHz)[a]	20 ± 20 (3)	19 ± 19 (4)	46 ± 32 (32)	2.5 ± 0.5 (0.04)
6 (229 GHz)	25.4 ± 0.6 (0.4)	23.4 ± 0.6 (0.4)	69 ± 7 (7)	11.5 ± 2.3 (0.09)

Notes. Parameters are derived from elliptical Gaussian fits to the image data described in Table 1. The error bars on the measured quantities include formal, systematic, and calibration uncertainties, as described in the appendix. For measured quantities, the value in parentheses indicates the contribution to the total error budget from formal fit uncertainties.
[a] After accounting for systematic errors, Mira B is formally indistinguishable from a point source in the Band 3 data.

envelope is highly structured on the scales that are relevant here (e.g., Mayer et al. 2011; Ramstedt et al. 2014).

4.2. Evidence for Non-uniformities on the Surface of Mira A

The high spatial resolution, high S/N, and good *u–v* coverage of the three data sets presented here allow the most detailed investigation to date of the brightness distribution on the radio surface of Mira A. In Figure 5 we present plots of the azimuthally averaged visibilities as a function of baseline length for the three observed frequencies. Overplotted as thick black lines are the best-fitting uniform elliptical disk models as presented in Table 2. Models of circular uniform disks are overplotted in red. The solid red line is a circular model with a disk diameter equal to the major axis of the best-fitting elliptical model, while the dashed line has a diameter equal to the minor axis of the best-fitting elliptical model.

We see that a simple uniform disk model does not provide a fully adequate characterization of the data at any of the three observed frequencies. At 46 and 96 GHz, the uniform disk model slightly over-predicts the measured visibility at *u-v* spacings near 1–2 Mλ and 0.5–1 Mλ, respectively, while under-predicting the values on the longest baselines. Deviations from the uniform elliptical disk model are also evident at 229 GHz, with the model fitting poorly across the longest baselines and the deviations showing a high level of significance. To see this effect in the image plane, in Figure 6 we plot the 229 GHz contours for Mira A over an image formed by subtracting the best-fitting elliptical disk model in the visibility domain and imaging the residuals. We also produced an analogous image by differencing a deconvolved image of the real data with a deconvolved image of the best uniform disk model, and the result is virtually indistinguishable, suggesting that the image residuals are not solely artifacts of the deconvolution process or limited image fidelity. Contamination from a spectral line within our band can also be excluded as a likely cause of the apparent brightness non-uniformity, as oxygen-rich red giants typically contain only a handful of weak molecular lines over the observed bandwidth (Tenenbaum et al. 2010; Kamiński et al. 2013).

We attempted to improve the fits to the visibility data using models that include components in addition to the uniform disk, including a ring (emulating limb brightening), a point source, or a Gaussian. For the 46 and 96 GHz data, we were unable to meaningfully constrain models including additional components, and none of these three simple models produced a significant improvement in the fit (as assessed by visual inspection of the residuals and the improvement in the χ^2 statistic). However, for the 229 GHz data, two-component models produced a clear improvement in χ^2, with the elliptical disk+Gaussian fit providing the best match to the data (Figure 7). A fit with a disk plus two point sources was also attempted, but was less satisfactory than the elliptical disk+Gaussian fit and required an additional free parameter.

For the elliptical disk+Gaussian model shown in Figure 7, the PA of the disk component was fixed at 144°.4 (i.e., to the value found originally from fitting a disk model without additional components; see Table 2). The total flux density in this model was 151 mJy, with 39% in a Gaussian component with FWHM 26 mas and a minor-to-major axis ratio of 0.92, centered 3.5 mas southwest of the nominal disk center, i.e., at the location of the bright region visible in Figure 6. In this model, the major and minor axes of the disk component are 13% larger and 2% smaller, respectively, compared with the fit given in Table 2. While the elliptical disk+Gaussian model is not unique, its success nonetheless underscores that the observed visibilities point to a nonuniform, asymmetric brightness distribution.

In its simplest form, the radio photosphere model of RM97 is not expected to exhibit a temperature inversion with increasing height, although the dissipation of energy from shocks could potentially lead to a region of increased temperature and level of ionization just above the radio photosphere. Such a region is expected to become detectable at millimeter and submillimeter wavelengths and may manifest itself as detectable limb brightening. While the present data do not rule out the presence of a chromosphere-like region, the fits presented in Figure 7 suggest that models without azimuthally symmetric limb brightening are able to reproduce the data equally well, or better than models that include it.

5. DISCUSSION

We have found excellent agreement between the newly observed millimeter wavelength flux densities for Mira A and the radio photosphere model of RM97 (Figure 4), offering strong observational support for this model and its extension to higher frequencies. However, we note that our current measurement of the flux density of Mira A at 46 GHz is somewhat higher than previous measurements at comparable frequencies. Based on 43 GHz data taken on 2000 October 26, Reid & Menten (2007) measured $S_{43\,GHz} = 4.8 \pm 0.2$ mJy, while based on data from 2005, Matthews & Karovska (2006) reported values of 2.44 ± 0.44 mJy (on May 17) and 2.61 ± 0.37 mJy (on June 28). Matthews & Karovska did not have available simultaneous measurements of the SiO maser to use for phase self-calibration (see Section 3.1), and we estimate that decorrelation losses resulting from the larger residual phase

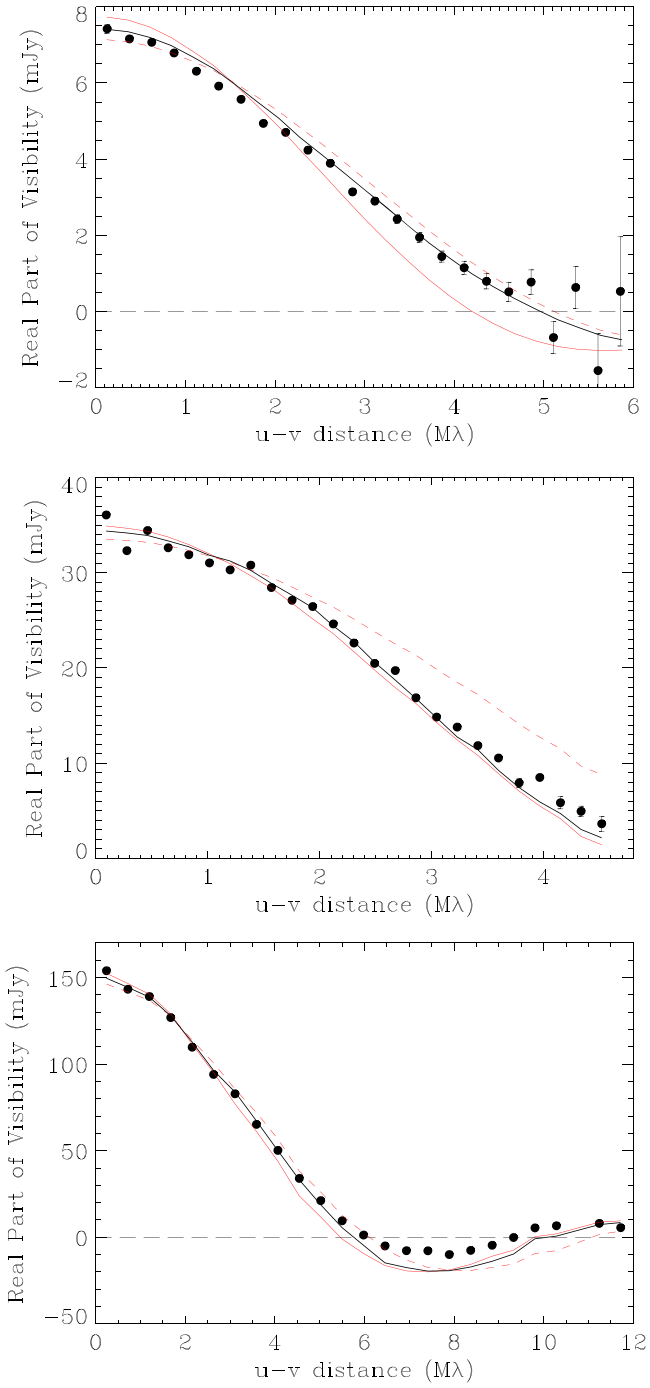

Figure 5. Visibility vs. baseline length for the three data sets presented in this paper: 46 GHz (top); 94 GHz (middle); 229 GHz (bottom). The solid black line shows the best-fitting uniform elliptical disk model from Table 2. The red lines represent circular uniform disk models with diameters equal to the major axes (solid lines) and minor axes (dashed lines) of the elliptical disk fits.

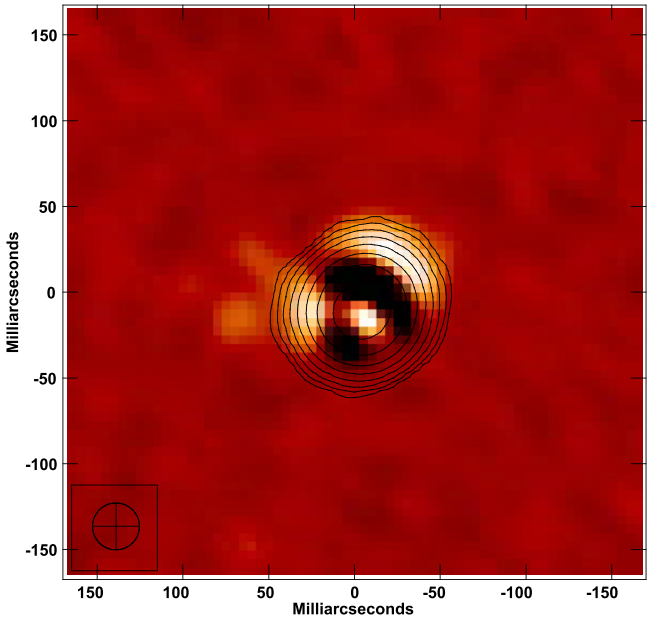

Figure 6. Contour map of the 229 GHz emission from Mira A (reproduced from Figure 3), overplotted on an image of the residuals after subtraction of the best-fitting uniform elliptical disk model. The residuals range from −1.4 to +0.9 mJy beam^{-1}, with the peak positive residual lying slightly southwest of the nominal disk center. In comparison, the peak surface brightness of the observed stellar emission is 71.1 mJy beam^{-1}. The restoring beam (FWHM 27.3 mas) is indicated in the lower left corner.

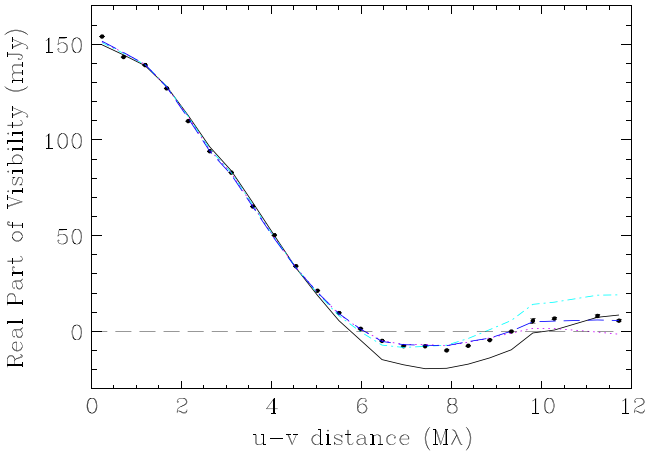

Figure 7. Same as Figure 5(c), but with additional models overplotted. The black solid line is the uniform elliptical disk model from Table 1. The colored lines show models that include a uniform elliptical disk plus an additional component: disk+point source (turquoise dash–dot line line); disk+ring (purple dotted line); disk+Gaussian (blue dashed line).

scatter in their data may have led to amplitude losses as high as ∼30%. Nonetheless, even accounting for this effect, as well as uncertainties in the absolute flux density scale of up to 20% (typical of measurements at this frequency), these data and the earlier measurement of Reid & Menten still appear to be consistent with a lower 43 GHz flux density for Mira A compared with our latest measurement.

The measurements of Reid & Menten (2007) and Matthews & Karovska (2006) were all obtained near a stellar phase $\phi \sim 0$ (i.e., near maximum optical light). Thus while an evolution in the radio and millimeter flux density of Mira over timescales of several years cannot be excluded, another possibility is that the radio flux density varies over the course of the stellar pulsation cycle. Indeed, previous 8.5 GHz measurements by RM97 at several phases during the pulsation cycle of Mira implied flux density variations of ∼15% at that frequency and hinted at a flux density minimum near $\phi = 0$. RM97 showed that such a trend could be reproduced by a radio photosphere model with low-level shocks (propagation speeds ∼10 km s^{-1}; see also Reid & Goldston 2002). Additional high-cadence monitoring at radio and millimeter wavelengths is clearly needed to settle the question of whether Mira's radio

flux density varies appreciably over the course of the stellar pulsation cycle, over longer timescales (several years), or both. Further, simultaneous monitoring at several frequencies, including longer wavelengths where the stellar disk is unresolved, would help to distinguish apparent brightness variations caused by uncertainties in the absolute flux density calibration of the JVLA and ALMA at millimeter wavelengths. Calibration at these wavelengths, particularly for long baseline measurements, is notoriously difficult since most strong, compact radio sources are highly variable at these wavelengths, while planetary sources, despite having well determined millimeter flux densities, become resolved on long baselines (see RM97 for additional discussion).

Both the size and ellipticity that we measure for Mira's radio photosphere at 46 GHz are consistent with the values previously measured at 43 GHz by Reid & Menten (2007), although the PA measured by those authors ($+39° \pm 50°$) deviates from our more recent value. This hints at the possibility that the shape of the photosphere may change with time. However, given the large formal uncertainty in the earlier PA measurement, this difference is only marginally significant, and additional measurements will be needed to confirm this possibility and to place constraints on the timescale of any such changes. New data sets of the quality that we present here would also permit searches for temporal variations as small as ~10% in the photospheric radius, even allowing for uncertainties caused by possible brightness non-uniformities in the stellar emission. Previous measurements in the near- and mid-infrared have already shown evidence of radius variations of this magnitude in Mira over the course of the stellar pulsation cycle (~10%; Weiner et al. 2003; Woodruff et al. 2004).

Measurements at other wavelengths have also supported the existence of an elongation of Mira's photosphere comparable to the one we measure at millimeter wavelengths. For example, $\epsilon \approx 0.85$ has been reported based on optical studies (Karovska et al. 1991; Wilson et al. 1992), although those studies suggest that the PA of the elongation varies with time. Using *Hubble Space Telescope* ultraviolet imaging data, Karovska et al. (1997) also reported an elongation along PA $\approx 175°$ (see also Karovska et al. 2005), while Tatebe et al. (2008) showed that measurements 11.15 μm are consistent with an ellipticity $\epsilon \sim 0.9$ along PA $\approx 169°$.

There are several possible causes for non-circular shapes of radio photospheres, including the presence of a close binary companion (see Mauron et al. 2013), non-radial pulsations, rotation, or magnetic fields. Our present data do not yet offer strong constraints on these various possibilities, but this is expected to change as more extensive databases of radio photosphere measurements become available from the JVLA and ALMA in the coming years.

A simple calculation suggests that the tidal force exerted by Mira B would be insufficient to cause a distortion of the observed magnitude. One may calculate an order of magnitude estimate of the change in radius or "tidal bulge", ΔR, raised by the presence of a perturbing potential along a line between the center-of-mass of the two bodies as:

$$\Delta R = \frac{m_2}{m_1}\left(\frac{R}{s}\right)^3 R, \quad (2)$$

where m_1 is the mass of the primary body, m_2 is the mass of the perturber, R is the radius of the star, and s is the separation between the two bodies (e.g., Danby 1992). Assuming $m_1 = 2.5\,M_\odot$ and $m_2 = 0.6\,M_\odot$ (Prieur et al. 2002), $R = 4 \times 10^{13}$ cm (Section 4.1.1), and $s = 100$ AU (Prieur et al.), then $\Delta r \approx 2 \times 10^8$ cm. This implies an ellipticity $\epsilon \sim 5 \times 10^{-6}$, several orders of magnitude smaller than observed. One possibility is that Mira has an additional unseen companion at a much smaller orbital radius. We also note that more sophisticated magnetohydrodynamic simulations have shown that a mechanism known as wind Roche-Lobe overflow may impose significant asymmetries on the shape of Mira's wind despite the large separation between the binary components (Mohamed & Podsiadlowski 2012). In the simulations of Mohamed & Podsiadlowski, distortion is seen in the dust shells as close as 10 AU from the star, although this study does not specifically address the magnitude of any expected distortion on the radio photosphere, which lies interior to the wind launch region.

Both observations (e.g., Cotton et al. 2006) and theoretical modeling (Thirumalai & Heyl 2013) point to magnetic fields as being important in the atmospheric dynamics of Mira and in AGB stars in general (see review by Vlemmings 2014). Future contemporaneous measurements of radio photospheres and maser emission from various species and transitions would be a powerful combination for constraining the roles of magnetic fields and their roles in shaping both the photosphere and the stellar outflow over larger scales (see also Gray et al. 2009; Amiri et al. 2012).

The data we have presented here have shown compelling evidence of a nonuniform, asymmetric brightness distribution on the radio-emitting surface of Mira. Evidence for brightness asymmetries on Mira has also been reported previously based on data at a variety of other wavelengths (Haniff et al. 1995; Karovska et al. 1999; Stewart et al. 2015). Lim et al. (1998) also showed that the red supergiant Betelgeuse (α Ori) exhibits large-scale irregularities in its radio surface (see also Richards et al. 2013). A likely cause of these brightness asymmetries are large-scale convective cells, which are expected to be present on the surfaces of both AGB stars and red supergiants (Schwarzschild 1975; Chiavassa et al. 2015).

6. CONCLUSIONS

Using data obtained with the JVLA and ALMA, we have presented resolved measurements of the millimeter wavelength continuum emission from both components of the Mira AB binary system at 46 GHz (7 mm), 96 GHz (3 mm), and 229 GHz (1 mm). The millimeter wavelength flux densities measured for Mira A are consistent with the radio photosphere model previously derived by RM97. A comparison with previously published measurements of Mira A at 43 GHz suggests that its flux density may vary over the course of the stellar pulsation cycle and/or on timescales of years. However, additional measurements are needed to confirm this possibility. The emission from Mira B is consistent to first order with free–free emission from a circumstellar hypercompact H II region of radius $\approx 2 \times 10^{13}$ cm, although the millimeter spectrum exhibits an unexpected upturn at higher frequencies, implying that a more complex model is needed to fully describe the emission.

The stellar disk of Mira A is resolved at all three observed frequencies. We measure a mean photospheric radius of ~3.0 AU at 46 GHz and find that the radius decreases systematically with increasing frequency, as expected if the

opacity decreases at shorter wavelengths. The shape of the radio photosphere of Mira exhibits an elongation, with a flattening of ∼10%–20%. It is presently unclear whether the shape and/or the direction of the elongation evolves with time.

The data presented here reveal evidence of brightness non-uniformities on the radio-emitting surface of Mira A. The cause of these non-uniformities may be large-scale convective cells, similar to what has been previously proposed to explain the surface irregularities on the supergiant Betelgeuse.

Note added in proof: after this paper was submitted, an independent analysis of the ALMA data for Mira AB by Vlemmings et al. (2015) was submitted and accepted for publication. The analysis of the ALMA data by these authors differs from our own in that for each ALMA band, Vlemmings et al. analyzed the data from the individual observing dates separately, and they adopted slightly different flux densities for the ALMA Band 3 flux calibrators. They also performed their imaging and data analysis using CASA and a stand-alone *u–v* fitting program rather than AIPS. The Vlemmings et al. study independently confirms evidence for a hot spot on Mira A and shows that the radio-emitting surface of Mira B has now been resolved. However, there are also some notable differences between our findings. First, based on the results of fits to the Band 3 visibility data, there are statistically significant differences in the size and PA for Mira A between our respective studies; indeed, Vlemmings et al. derive a smaller size for Mira A in Band 3 than in Band 6, the opposite of what we report here. This in turn leads to a rather different estimate for the Band 3 brightness temperature. While the respective sizes that we derive for Mira A in Band 6 agree to within uncertainties, the PA of the major axis differs by more than 90°. We note that our value is consistent with the visible elongation of the star in the image plane (e.g., Figure 3). Another important distinction between our results is that Vlemmings et al. report a shallower spectral index for Mira A than we have advocated in the present work. They also find evidence that the spectral index changes significantly between 94 and 229 GHz. In contrast, we have found a single spectral index of $\alpha = 1.86$ (i.e., the value predicted by the radio photosphere model of MR97) to be consistent with recent measurements between 46 and 338 GHz. Lastly, while both of our studies have revealed evidence for the presence of a hot spot on Mira A at approximately the same location, Vlemmings et al. report a larger peak residual for this feature after subtracting the best uniform disk fit and infer a smaller size for the spot. However, since the inferred size of this feature is only a fraction of the synthesized beam, its size, and hence its inferred brightness temperature, are necessarily rather uncertain.

The authors thank T. Kamiński for valuable discussions and E. Greisen for developments in AIPS that aided this work. The JVLA observations presented here were part of NRAO program 14A-026. This paper makes use of the following ALMA data: ADS/JAO.ALMA #2011.0.00014.SV. ALMA is a partnership of ESO (representing its member states), NSF (USA), and NINS (Japan), together with NRC (Canada) and NSC and ASIAA (Taiwan), in cooperation with the Republic of Chile. The Joint ALMA Observatory is operated by ESO, AUI/NRAO and NAOJ. The National Radio Astronomy Observatory is a facility of the National Science Foundation operated under cooperative agreement by Associated Universities, Inc.

APPENDIX
CALCULATION OF UNCERTAINITIES FOR MEASURED QUANTITIES

The error bars quoted for the measured quantities in Tables 2 and 3 contain contributions from both formal fitting uncertainties and systematic errors, where the total error is assumed to be $\sigma_t = (\sigma_f^2 + \sigma_s^2)^{0.5}$. The term σ_f was taken to be the uncertainties reported by the AIPS JMFIT and OMFIT tasks that were used for fitting Gaussian and uniform disk models, respectively, and which compute uncertainties according to the formalism outlined by Condon (1997). The systematic errors, σ_s, that affect our measurements include terms resulting from blurring of the images from phase fluctuations on long baselines (i.e., "seeing" effects; hereafter $\sigma_{s,p}$), as well as contributions that are difficult to quantify from first principles (hereafter $\sigma_{s,o}$), such as those caused by the limited sampling of the *u–v* plane, by the size and shape of the interferometer dirty beam, and by the gridding and deconvolution process.

Assuming that the residual phase noise on long baselines arises from tropospheric phase fluctuations that follow a Gaussian distribution, then the true size of a source will be affected by convolution with a Gaussian whose FWHM is given by $\theta_p = a\sqrt{8(\ln 2)}$, where $a = \sigma_\phi \lambda/(2\pi b)$ (Thompson et al. 1994). Here σ_ϕ represents the rms phase fluctuation on a baseline of projected length b. For the JVLA data ($\lambda \approx 7$ mm) we find $\sigma_\phi \approx 29°$ for the three longest baselines ($b = 34.5$ km), implying $\theta_p \approx 7.5$ mas. For the ALMA Band 3 data ($\lambda \approx 3$ mm), $\sigma_\phi \approx 75°$ on a baseline with $b = 10.66$ km, implying $\theta_p \approx 29$ mas. Finally, for ALMA Band 6 ($\lambda \approx 1.3$ mm), $\sigma_\phi \approx 96°$ for b=15.2 km, implying $\theta_p \approx 4.7$ mas. Consequently, for our size measurements we include in the error budget a relative error term $\sigma_{s,p} = \left[\theta_m - \sqrt{\theta_m^2 - \theta_p^2}\right] \Big/ \theta_m$ where θ_m is the measured major or minor axis FWHM. Phase noise also causes a decrease in the correlated amplitude on the longest baselines of magnitude $\exp(-\sigma_\phi^2/2)$ (e.g., Thompson et al.). However, the effect on the total integrated flux density of the source in our case is quite small, and we have neglected this effect.

To obtain an estimate of additional contributions $\sigma_{s,o}$ to the total systematic error budget, we performed a series of numerical experiments. As an initial test, we constructed a series of one-dimensional (1D) Gaussian signals, added to them different levels of random noise, and measured the apparent FWHM. We then deconvolved the apparent width from the "true" width by subtracting in quadrature a Gaussian representing various observing resolutions to yield an intrinsic FWHM. Finally, based on series of 1000 trials for each combination of parameters (which bracketed the range of S/N and source-to-beam size ratios encountered in our real data), we computed the rms dispersion in the inferred signal width. In this way we have obtained a lower limit to the expected systematic uncertainty in the measured source sizes.

In a second series of experiments, we introduced into our actual visibility data at each frequency a series of artificial elliptical Gaussians and uniform elliptical disks, offset by −0.25 and −1.0 arcsec south of the phase center, respectively. For the Gaussian sources, we set the flux density and axial ratio

to the values measured from our fits to Mira A (Table 2), but we systematically varied the PA from −90° to +90°, in increments of 15°. For the uniform elliptical disks, we performed trials using disk major and minor axes equal to our measured values from Table 2, but again varied the PAs over several different values. We then measured the parameters of the artificial Gaussians in deconvolved images using JMFIT and of the artificial disks in the visibility domain using OMFIT, respectively, and compared these numbers with the expected values.

Not surprisingly, we found the errors on the source sizes to be comparable to, or slightly higher in our 2D experiments compared with those derived from our initial 1D experiments. We also found that the 2D Gaussian fits tended to systematically underestimate the expected source flux density and size, typically by a few per cent. This effect persisted even if smaller cell sizes were used to compute the deconvolved images. This effect may therefore arise in part from the intrinsically non-Gaussian shape of the real interferometer beam and/or deconvolution biases.

Based on the above numerical experiments, we adopt as $\sigma_{s,o}$ for the image plane and visibility domain measurements, respectively, the mean error in each measured quantity from all of the 2D trials at each of the three frequencies. For the sources sizes, the *total* systematic error includes contributions both from $\sigma_{s,o}$ and $\sigma_{s,p}$ and is taken to be $\sigma_s = (\sigma_{s,p}^2 + \sigma_{s,o}^2)^{0.5}$. In the case of the flux density, we have additionally included contributions to the systematic error budget from pointing uncertainties and absolute flux density calibration (assumed to contribute relative errors of 1% and 20%, respectively, at all three observed frequencies).

For Mira A, the uncertainties on the source size and PA reported in this work are dominated by systematic uncertainties, whereas for the weaker radio source Mira B, statistical errors dominate at two of the three observed frequencies. For both stars, the uncertainty in the integrated flux density is dominated by the absolute calibration uncertainty inherent at millimeter wavelengths.

REFERENCES

ALMA Partnership, Fomalont, E. B., Vlahakis, C., et al. 2015, ApJL, in press (arXiv:1504.04877)
Amiri, N., Vlemmings, W. H. T., Kemball, A. J., & van Langevelde, H. J. 2012, A&A, 538, A136
Chiavassa, A., & Freytag, B. 2015, in Why Galaxies Care about AGB Stars III, ed. F. Kerschbaum, J. Hron & R. Wing, in press (arXiv:1410.3868)
Condon, J. J. 1997, PASP, 109, 166
Cotton, W. D. 2008, PASP, 120, 439
Cotton, W. D., Vlemmings, W., Mennesson, B., et al. 2006, A&A, 456, 339
Danby, J. M. A. 1992, Fundamentals of Celestial Mechanics (2nd ed.; Richmond: Willmann-Bell)
Feast, M. W., Glass, I. S., Whitelock, P. A., & Catchpole, R. M. 1989, MRNAS, 241, 375
Gray, M. D., Wittkowski, M., Scholz, M., et al. 2009, MNRAS, 394, 51
Greisen, E. W. 2003, in Information Handling Astronomy—Historical Vistas, ed. A. Heck (Dordrecht: Kluwer), 109
Haniff, C. A., Scholz, M., & Tuthill, P. G. 1995, MNRAS, 276, 640
Kamiński, T., Gottlieb, C. A., Menten, K. M., et al. 2013, A&A, 551, A113
Karovska, M. 1999, in IAU Symp. 191, Asymptotic Giant Branch Stars, ed. T. Le Bertre, A. Lébre & C. Waelkens (San Francisco, CA: ASP), 139
Karovska, M., Hack, W., Raymond, J., & Guinan, E. 1997, ApJL, 482, L175
Karovska, M., Nisenson, P., Papaliolios, C., & Boyle, R. P. 1991, ApJL, 374, L51
Karovska, M., Schlegel, E., Hack, W., Raymond, J. C., & Wood, B. E. 2005, ApJL, 623, L137
Lim, J., Carilli, C. L., White, S. M., Beasley, A. J., & Marson, R. G. 1998, Natur, 392, 575
Matthews, L. D., & Karovska, M. 2006, ApJL, 637, L49
Mauron, N., Huggins, P. J., & Cheung, C.-L. 2013, A&A, 551, A110
Mayer, A., Jorissen, A., Kerschbaum, F., et al. 2011, A&A, 531, L4
McIntosh, G. C., & Bonde, J. 2010, PASP, 122, 396
Menten, K. M., Reid, M. J., Kamiński, T., & Claussen, M. J. 2012, A&A, 543, A73
Mohamed, S., & Podsiadlowski, P. 2012, BaltA, 21, 88
Pearson, T. J. 1999, in ASP Conf. Ser. 180, Synthesis Imaging in Radio Astronomy II, ed. G. B. Taylor, C. L. Carilli & R. A. Perley (ASP: San Francisco, CA), 335
Perley, R. A., & Butler, B. J. 2013, ApJS, 204, 19
Perley, R. A., Chandler, C. J., Butler, B. J., & Wrobel, J. M. 2011, ApJ, 739, 1
Perrin, G., Ridgway, S. T., Mennesson, B., et al. 2004, A&A, 426, 279
Prieur, J. L., Aristidi, E., Lopez, B., et al. 2002, ApJS, 139, 249
Ramstedt, S., Mohamed, S., Vlemmings, W. H. T., et al. 2014, A&A, 570, L14
Reid, M. J., & Goldston, J. E. 2002, ApJ, 568, 931
Reid, M. J., & Menten, K. M. 1990, ApJL, 360, L51
Reid, M. J., & Menten, K. M. 1997, ApJ, 476, 327
Reid, M. J., & Menten, K. M. 2007, ApJ, 671, 2068
Richards, A. M. S., Davis, R. J., Decin, L., et al. 2013, MNRAS, 432, L61
Ryde, N., & Schöier, F. L. 2001, ApJ, 547, 384
Schwarzschild, M. 1975, ApJ, 195, 137
Seaquist, E. R., Taylor, A. R., & Button, S. 1984, ApJ, 284, 202
Sokoloski, J. L., & Bildsten, L. 2010, ApJ, 723, 1188
Stewart, P. N., Tuthill, P. G., Nicholson, P. D., Hedman, M. M., & Lloyd, J. P. 2015, MNRAS, 449, 1760
Tatebe, K., Wishnow, E. H., Ryan, C. S., et al. 2008, ApJ, 689, 1289
Taylor, A. R., & Seaquist, E. R. 1984, ApJ, 286, 263
Tenenbaum, E. D., Dodd, J. L., Milam, S. N., Woolf, N. J., & Ziurys, L. M. 2010, ApJS, 190, 348
Thirumalai, A., & Heyl, J. S. 2013, MNRAS, 430, 1359
Thompson, A. R., Moran, J. M., & Swenson, G. W., Jr. 1994, Interferometry and Synthesis in Radio Astronomy (Malabar, FL: Krieger)
Trippe, S., Neri, R., Krips, M., et al. 2010, A&A, 515, 40
Vlemmings, W. H. T. 2014, in in IAU Symp. 302, Magnetic Fields throughout Stellar Evolution, ed. P. Petit, M. Jardine & H. Spruit (Cambridge: Cambridge Univ. Press), 389
Vlemmings, W. H. T., Ramstedt, S., O'Gorman, E., et al. 2015, A&A, 577, L4
Weiner, J., Hale, D. D. S., & Townes, C. H. 2003, ApJ, 588, 1064
Wilson, R. W., Baldwin, J. E., Buscher, D. F., & Warner, P. J. 1992, MNRAS, 257, 369
Woodruff, H. C., Eberhardt, M., Driebe, T., et al. 2004, A&A, 421, 703
Wootten, A., & Thompson, A. R. 2009, IEEEP, 97, 1463